

## **Performance Improvement for double-stator permanent magnet synchronous machine using analytical subdomain model**

**DOI : 10.36909/jer.ICEPE.19567**

Mohd Saufi Ahmad<sup>1</sup>, Dahaman Ishak<sup>2\*</sup>, Tiang Tow Leong<sup>1</sup> and Mohd Rezal Mohamed<sup>3</sup>

<sup>1</sup>Faculty of Electrical Engineering Technology, Pauh Putra Campus, Universiti Malaysia Perlis, Arau, Perlis, Malaysia.

<sup>2</sup>School of Electrical and Electronic Engineering, Universiti Sains Malaysia, Nibong Tebal, Penang, Malaysia.

<sup>3</sup>Universiti Kuala Lumpur Malaysian Spanish Institute, Kulim, Kedah, Malaysia.

\* Corresponding Author: dahaman@usm.my

### **ABSTRACT**

An analytical subdomain model is employed in this paper for predicting the magnetic field distributions in a three-phase double-stator permanent magnet synchronous machine (DS-PMSM) during open-circuit and onload conditions. Due to the stator cores are located in the outer and inner parts of the motor, the DS-PMSM construction is quite complex. The rotor magnets are positioned between these two stators. The stator inner radius, stator outer radius, slot opening, magnet arc, magnet thickness, inner and outer air-gap thickness and number of windings turns will directly influence the motor performance in DS-PMSM. The analytical subdomain model employed in this paper has a significant advantage as a rapid design tool since it is capable of precisely predicting the performance of DS-PMSM while requiring less computational effort. The analytical model was initially created using the separation of variables technique in four subdomains based on the Poisson's and Laplace's equations: inner air-gap, inner magnet, outer magnet and outer air-gap. Applying the appropriate boundary and interface conditions yields the field solutions in each subdomain. Besides, the fractional DS-PMSM with different number of slots between outer and inner stators to rotor poles can result in low cogging torque and non-overlapping winding configuration. The analytical results are

validated by Finite Element Analysis (FEA). The slotted air-gap flux density, back-emf, and output torque have all been evaluated as electromagnetic performances. The results demonstrate that the suggested analytical model is capable of accurately predicting the DS-PMSM performance.

**Keywords:** Double-Stator; Synchronous Machine; Permanent Magnet; Analytical Subdomain Model.

## INTRODUCTION

Permanent magnet synchronous motors (PMSMs) are gaining traction in a variety of new applications due to excellent dynamic performance, high power density, high torque and high efficiency (Zhao et al. 2021; H. Wang et al. 2020; Wu and Zhu 2015). In general, the relationship between slots and poles has a significant role in deciding the form of windings to employ in PMSM design. Fractional slot configurations indicate that the motor windings are non-overlapping and single-wound tooth type, whereas non-fractional slot configurations indicate that the motor windings are overlapping and distributed type. The fractional slot motors, on the other hand, are more preferred because have a low cogging torque inherent in it, short end-windings, and a high fundamental winding factor. (Ahmad et al. 2020; Akmar Mohd-Shafri et al. 2020; Wu and Zhu 2015). The number of stator slots per rotor pole per phase,  $N_{spp}$ , is used to define fractional slot motors. Having  $N_{spp}$  lower than unity will typically equip the permanent magnet (PM) machines with coils that span one stator tooth of a stator for fractional slot motors (Edhah, Alsawalhi, and Al-Durra 2019). Besides, there are multiple PMSM topologies, each creating a specific layout of the rotor and stator windings. Due to its high flux-weakening and overload capability, the PM motor with fractional concentrated windings positioned is emerging as a possible candidate. (Awah et al. 2016). In these machines, the coils for each phase are concentrated and wound on independent stator teeth, preventing phase windings from overlapping. This is not only a rapid manufacturing advantage, but also provides to a higher copper packing factor, increased efficiency, and a

reduced risk of an interphase fault (J. Wang, Yuan, and Atallah 2013; Yang and Peng 2019). Due to the advantages of double stator permanent magnet synchronous machines (DS-PMSM) over conventional single stator PMSM, they have been the topic of substantial research in recent years. In (Zhu and Cheng 2019), the DS-PMSM is used in a wind energy generation system to cooling two spatially independent stators. A double-stator single-rotor has been created to lower manufacturing costs in machine constructions due to the relative location of both stator slots (Gul, Gao, and Lenwari 2020). The double-stator PMSM is proposed in (Z. Wang et al. 2019) for usage with electric vehicles (EVs) and dual-channel magnetically integrated charger operations. While additional DS-PMSM types have been researched for their potential to minimize mechanical stress and weight while keeping the same power density (Asef et al. 2018).

In general, the inner and outer stator slot numbers are same in DS-PMSM. However, this article investigates a DS-PMSM with different slot-to-pole ratios in the inner and outer stators. Despite the fact that the outer and inner stators have differing slot numbers, their ratios to the rotor pole remain fractional. As a result, the machine design proposed has a high winding factor. Numerical approaches like as finite element analysis (FEA) are widely used to design and establish the ideal configuration of DS-PMSMs before fabrication and manufacture. Manually varying the important parameters in the motor constructions, on the other hand, will require a longer computational burden, making it impractical to achieve the best motor performance (Ahmad et al. 2021; Mohamed and Ishak 2019).

Therefore, an analytical subdomain model can potentially provide a viable and faster solution for designing DS-PMSMs to address this issue. In this regard, this article presents an analytical sub-domain model for a three-phase DS-PMSM with different numbers of slots between the outer and inner stators, where the outer section has a 12-slot/10-pole slot-to-pole combination and the inner part has a 9-slot/10-pole combination.

## MOTOR GEOMETRY

The geometric structure of a double stator permanent magnet synchronous motor (DS-PMSM) is complicated. The outer part and inner part are the stator cores, while the rotor magnets are positioned between these two stators. Polyphase windings are then wound in both stators, with the outer and inner stator phase coils coupled in series or independently. Therefore, both stator windings might be treated as a single motor or as two distinct motors. The designed model of the three-phase DS-PMSM is illustrated in Figure 1. It consists of a 12-slot outer stator, a 10-pole rotor, and a 9-slot inner stator. Permanent magnets (PMs) mounted on the rotor core for inner and outer surfaces are employed. Non-overlapping double-layer windings are employed as the winding configuration for both the inner and outer stators.

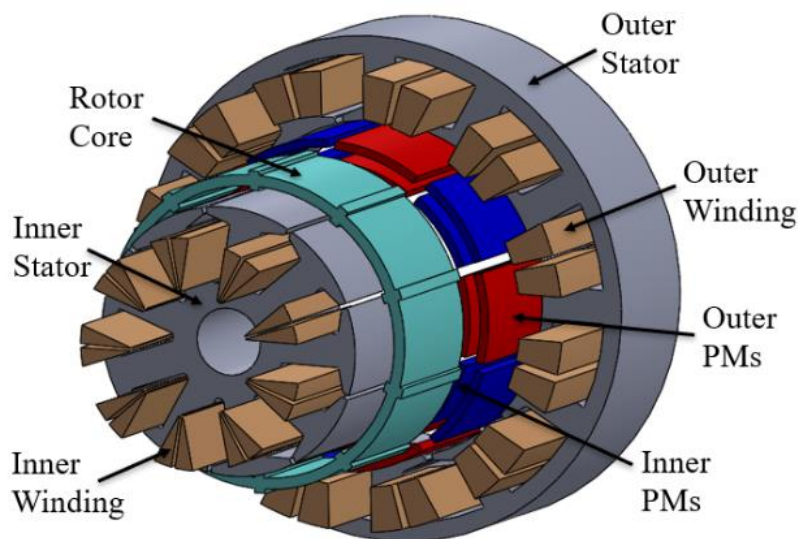


**Figure 1.** DS-PMSM Construction

Maximizing output torque and power per volume should be rigorously explored in any motor design work. Several motor parameters can greatly influence the motor performance. Those parameters include stator inner radius, stator outer radius, outer and inner airgap thickness, slot opening, stator tooth shape, stator yoke, stator tooth width, magnet shape, magnet arc, magnet thickness and number of turns for windings. Additionally, fractional slot winding or

integral slot winding should also be considered and contemplated into DS-PMSM design stage for achieving higher output torque. Some of these parameters may potentially be more dominant than others in generating higher torque and characterizing the motor performance. The motor parameters are illustrated in the Figure 2(a) for outer stator with permanent magnet rotor and Figure 2(b) for inner stator with permanent magnet rotor. In addition, the detail dimensions for the parameters are shown in Table 1.

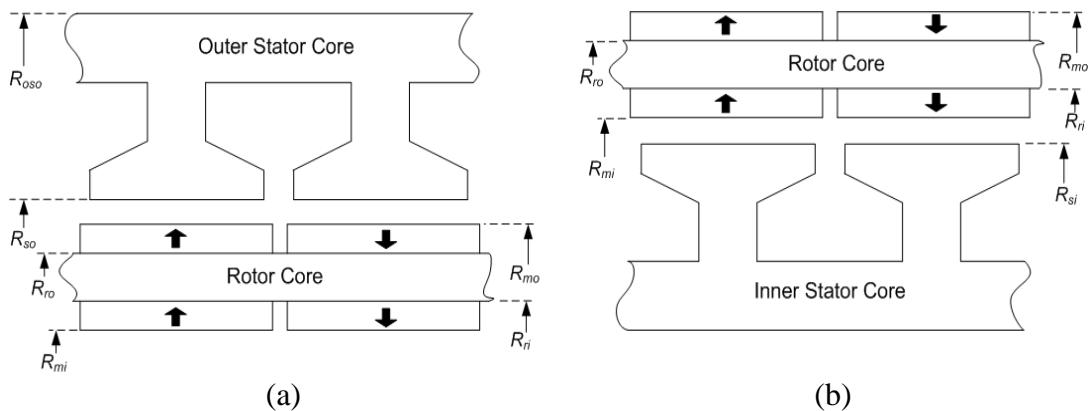


**Figure 2** DS-PMSM Parameters (a) Outer stator section (b) Inner stator section

**Table 1.** Dimensions of DS-PMSM.

Parameters	Symbol	Values
Inner Stator Slot Number	$N_{is}$	9
Outer Stator Slot Number	$N_{os}$	12
Rotor Pole Number	$2p$	10
Stack Length	$l_s$	40 mm
Inner Air-gap Length	$l_{ig}$	1 mm
Outer Air-gap Length	$l_{og}$	1 mm
Outer Magnet Thickness	$h_{om}$	3 mm
Inner Magnet Thickness	$h_{im}$	3 mm
Magnet Remanence	$B_r$	1.12 T
Saturation Flux density	$B_{max}$	1.6 T
Relative Permeability	$\mu_r$	1.05
Inner Stator Outer Radius	$R_{iso}$	48 mm
Inner Stator Inner Radius	$R_{isi}$	12 mm
Outer Stator Outer Radius	$R_{oso}$	90 mm
Outer Stator Inner Radius	$R_{osi}$	60 mm
Outer Magnet Outer Radius	$R_{omo}$	59 mm

Inner Magnet Inner Radius	$R_{imi}$	49 mm
Outer Rotor Radius	$R_{ro}$	59 mm
Inner Rotor Radius	$R_{ri}$	49 mm
Rated Speed Rotation	$r_m$	600 rpm
Outer Winding per coil	$N_{oc}$	114 turns
Inner Winding per coil	$N_{ic}$	50 turns

## ANALYTICAL FORMULATIONS AND FIELD SOLUTIONS

Parameters shown in Figure 2 are used in the formulation of the proposed analytical subdomain model (ASDM) for DS-PMSM. The ASDM are derived and formulated for estimating the characteristics of air gap magnetic fields in surface-mounted DS-PMSM which can account for the effects of slot opening, tooth tips, magnet span, magnet thickness, magnet shape, air gap thickness, magnet's magnetization patterns and fractional combinations of slot and pole numbers. The formulated analytical subdomain model uses 2D polar co-ordinate system and considers motor geometry having four subdomains which outer airgap, outer rotor magnets, inner rotor magnet, and inner airgap. These four regions of subdomain further will be marked as region I, II, III and IV. The magnetic potentials given by either Laplace's equation or Poisson's equation in each subdomain are obtained by the variable separation technique, whereas the radial component and tangential components of magnetic fields for each subdomain are solved by applying the appropriate boundary conditions and interfacing conditions. Therefore, the formulated analytical subdomain model would be able to predict accurately the airgap magnetic flux density distributions during open-circuit, armature reaction field and onload conditions. Initially, the magnetic flux density  $B$  and field intensity  $H$  in these four regions can be expressed in the following relationships

$$\text{As a region I,} \quad \vec{B}_I = \mu_o \vec{H}_I \quad (1)$$

$$\text{As a region II,} \quad \vec{B}_{II} = \mu_o \mu_r \vec{H}_{II} + \mu_o \vec{M} \quad (2)$$

$$\text{As a region III,} \quad \vec{B}_{III} = \mu_o \mu_r \vec{H}_{III} + \mu_o \vec{M} \quad (3)$$

$$\text{As a region IV, } \vec{B}_{IV} = \mu_o \vec{H}_{IV} \quad (4)$$

where  $\mu_r$  is relative permeability of PMs,  $\mu_o$  is permeability of free space and  $\vec{M}$  is the magnetization of PMs. In polar coordinates,  $\vec{M}$  is provided as

$$\vec{M} = \vec{M}_r r + \vec{M}_\theta \theta \quad (5)$$

$M_r$  and  $M_\theta$  donate the components of  $M$  at the radial and tangential magnetization distributions respectively. The magnetization distribution of  $M_r$  and  $M_\theta$  can be expended into a Fourier series components as

$$M_r = \sum_{n=1,3,5,\dots}^{\infty} M_{rn} \cos(np\theta) \quad (6)$$

$$M_\theta = \sum_{n=1,3,5,\dots}^{\infty} M_{\theta n} \sin(np\theta) \quad (7)$$

For radial magnetization in PMs,  $M_{\theta n}$  will always be zero and the component of  $M_{rn}$  can be represented as

$$M_{rn} = \frac{4}{n\pi} \frac{B_r}{\mu_o} \sin \frac{\alpha_p}{2} \quad (8)$$

The scalar magnetic potential is used to describe the magnetic fields in the airgap which governed by Laplace's equation, and the scalar magnetic potential in permanent magnet is governed by Quasi-poisson's equation. In this paper, the scalar magnetic potential will be expressed in four subdomain regions i.e. outer airgap  $\phi_I$ , outer PMs  $\phi_{II}$ , inner PMs  $\phi_{III}$  and inner airgap  $\phi_{IV}$ . The curl of the scalar magnetic potentials in each region is given by

$$\frac{\partial^2 \phi_I}{\partial r^2} + \frac{1}{r} \frac{\partial \phi_I}{\partial r} + \frac{1}{r^2} \frac{\partial^2 \phi_I}{\partial \theta^2} = 0 \quad (9)$$

$$\frac{\partial^2 \phi_{II}}{\partial r^2} + \frac{1}{r} \frac{\partial \phi_{II}}{\partial r} + \frac{1}{r^2} \frac{\partial^2 \phi_{II}}{\partial \theta^2} = \frac{1}{\mu_r} \text{div} \vec{M} \quad (10)$$

$$\frac{\partial^2 \phi_{III}}{\partial r^2} + \frac{1}{r} \frac{\partial \phi_{III}}{\partial r} + \frac{1}{r^2} \frac{\partial^2 \phi_{III}}{\partial \theta^2} = \frac{1}{\mu_r} \text{div} \vec{M} \quad (11)$$

$$\frac{\partial^2 \phi_{IV}}{\partial r^2} + \frac{1}{r} \frac{\partial \phi_{IV}}{\partial r} + \frac{1}{r^2} \frac{\partial^2 \phi_{IV}}{\partial \theta^2} = 0 \quad (12)$$

The derivative of permanent magnet magnetization vector  $M$  can be expressed as

$$\text{div} \vec{M} = \frac{M_r}{r} + \frac{\partial M_r}{\partial r} + \frac{1}{r} \frac{\partial M_\theta}{\partial \theta} = \sum_{n=1,3,5,\dots}^{\infty} \frac{1}{r} M_n \cos(np\theta) \quad (13)$$

where  $M_r$  and  $M_\theta$  donate the components of magnetization  $M$  at the radial and tangential magnetization distributions. By using separation of variable method, the general solutions of scalar magnetic potentials for each region can be expressed as

$$\phi_I(r, \theta) = \sum_{n=1,3,5,\dots}^{\infty} A_n r^{np} + B_n r^{-np} \cos(np\theta) \quad (14)$$

$$\phi_{II}(r, \theta) = \sum_{n=1,3,5,\dots}^{\infty} C_n r^{np} + D_n r^{-np} \cos(np\theta) + \sum_{n=1,3,5,\dots}^{\infty} \frac{M_n}{\mu_r [1-(np)^2]} r \cos(np\theta) \quad (15)$$

$$\phi_{III}(r, \theta) = \sum_{n=1,3,5,\dots}^{\infty} E_n r^{np} + F_n r^{-np} \cos(np\theta) + \sum_{n=1,3,5,\dots}^{\infty} \frac{M_n}{\mu_r [1-(np)^2]} r \cos(np\theta) \quad (16)$$

$$\phi_{IV}(r, \theta) = \sum_{n=1,3,5,\dots}^{\infty} G_n r^{np} + H_n r^{-np} \cos(np\theta) \quad (17)$$

where  $A_n, B_n, C_n, D_n, E_n, F_n, G_n$  and  $H_n$  are constants determined by applying the boundary condition. Interface between the inner and outer stator with the outer and inner airgaps in this DS-PMSMs can be represented by following boundary condition equations. For outer part with the outer air-gap, the boundary conditions are satisfied by

$$H_{\theta I}(r, \theta)|_{r=R_{so}} = 0 \quad (18)$$

$$H_{\theta II}(r, \theta)|_{r=R_{so}} = 0 \quad (19)$$

$$B_{rI}(r, \theta)|_{r=R_{mo}} = B_{rII}(r, \theta)|_{r=R_{mo}} \quad (20)$$

$$H_{\theta I}(r, \theta)|_{r=R_{mo}} = H_{\theta II}(r, \theta)|_{r=R_{mo}} \quad (21)$$

whereas for inner part with the inner air-gap, the boundary conditions are satisfied by

$$B_{rIII}(r, \theta)|_{r=R_{mi}} = B_{rIV}(r, \theta)|_{r=R_{mi}} \quad (22)$$

$$H_{\theta III}(r, \theta)|_{r=R_{mi}} = H_{\theta IV}(r, \theta)|_{r=R_{mi}} \quad (23)$$

$$H_{\theta III}(r, \theta)|_{r=R_{si}} = 0 \quad (24)$$

$$H_{\theta IV}(r, \theta)|_{r=R_{ri}} = 0 \quad (25)$$

Applying the abovementioned interface and boundary conditions, the constant coefficient can be determined and furthermore by solving the general solutions consisting of Laplacian and Poissonian equations within the boundary conditions (Ling, Ishak, and Tiang 2017; Tiang et al. 2015) the equations (26) and (27) will be represent the radial and tangential components of the flux density in polar coordinates for the slotted DS-PMSM in the outer airgap, whereas equations (28) and (29) explain the inner airgap.

$$B_{rI}(r, \theta) = \sum_{n=1,3,5,\dots}^{\infty} \frac{\mu_o M_n}{\mu_r} \frac{np}{(np)^2 - 1} \cdot \left\{ \frac{2 \left(\frac{R_{ro}}{R_{mo}}\right)^{np+1} + (np-1) - (np+1) \left(\frac{R_{ro}}{R_{mo}}\right)^{2np}}{\frac{\mu_r+1}{\mu_r} \left[1 - \left(\frac{R_{ro}}{R_{so}}\right)^{2np}\right] - \frac{\mu_r-1}{\mu_r} \left[\left(\frac{R_{mo}}{R_{so}}\right)^{2np} - \left(\frac{R_{ro}}{R_{ri}}\right)^{2np}\right]} \right\} \cdot \left[ \left(\frac{r_o}{R_{so}}\right)^{np-1} \left(\frac{R_{mo}}{R_{so}}\right)^{np+1} + \left(\frac{R_{mo}}{r_o}\right)^{np+1} \right] \cdot \cos np\theta \quad (26)$$

$$B_{\theta I}(r, \theta) = \sum_{n=1,3,5,\dots}^{\infty} -\frac{\mu_o M_n}{\mu_r} \frac{np}{(np)^2 - 1} \cdot \left\{ \frac{2 \left(\frac{R_{ro}}{R_{mo}}\right)^{np+1} + (np-1) - (np+1) \left(\frac{R_{ro}}{R_{mo}}\right)^{2np}}{\frac{\mu_r+1}{\mu_r} \left[1 - \left(\frac{R_{ro}}{R_{so}}\right)^{2np}\right] - \frac{\mu_r-1}{\mu_r} \left[\left(\frac{R_{mo}}{R_{so}}\right)^{2np} - \left(\frac{R_{ro}}{R_{ri}}\right)^{2np}\right]} \right\} \cdot \left[ \left(\frac{r_o}{R_{so}}\right)^{np-1} \left(\frac{R_{mo}}{R_{so}}\right)^{np+1} - \left(\frac{R_{mo}}{r_o}\right)^{np+1} \right] \cdot \cos np\theta \quad (27)$$

$$B_{rIV}(r, \theta) = \sum_{n=1,3,5,\dots}^{\infty} -\frac{\mu_o M_n}{\mu_r} \frac{np}{(np)^2 - 1} \cdot \left\{ \frac{(np-1) \left(\frac{R_{mi}}{R_{ri}}\right)^{2np} + 2 \left(\frac{R_{mi}}{R_{ri}}\right)^{np-1} - (np+1)}{\frac{\mu_r+1}{\mu_r} \left[1 - \left(\frac{R_{si}}{R_{ri}}\right)^{2np}\right] - \frac{\mu_r-1}{\mu_r} \left[\left(\frac{R_{si}}{R_{mi}}\right)^{2np} - \left(\frac{R_{mi}}{R_{ri}}\right)^{2np}\right]} \right\}$$

$$\cdot \left[ \left( \frac{r_i}{R_{mi}} \right)^{np-1} + \left( \frac{R_{si}}{R_{mi}} \right)^{np-1} \left( \frac{R_{si}}{r_i} \right)^{np+1} \right] \cdot \cos np\theta \quad (28)$$

$$B_{\theta IV}(r, \theta) = \sum_{n=1,3,5,\dots}^{\infty} -\frac{\mu_o M_n}{\mu_r} \frac{np}{(np)^2-1} \cdot \left\{ \frac{(np-1) \left( \frac{R_{mi}}{R_{ri}} \right)^{2np} + 2 \left( \frac{R_{mi}}{R_{ri}} \right)^{np-1} - (np+1)}{\mu_r + 1 \left[ 1 - \left( \frac{R_{si}}{R_{ri}} \right)^{2np} \right] - \mu_r - 1 \left[ \left( \frac{R_{si}}{R_{mi}} \right)^{2np} - \left( \frac{R_{mi}}{R_{ri}} \right)^{2np} \right]} \right\} \\ \cdot \left[ \left( \frac{R_{si}}{R_{mi}} \right)^{np-1} \left( \frac{R_{si}}{r_i} \right)^{np+1} - \left( \frac{r_i}{R_{mi}} \right)^{np-1} \right] \cdot \cos np\theta \quad (29)$$

where all parameters are defined and given in the Table 1. Based on flux density distribution at both airgaps, the back-emf induced by each phase can be determined by

$$\mathcal{E}_{phase} = 2N_p l_a R_{osi} \omega_r \sum_{n=1,3,5,\dots}^{\infty} B_{rI}(r, \theta) K_{dpon} \sin np\theta \\ + 2N_p l_a R_{iso} \omega_r \sum_{n=1,3,5,\dots}^{\infty} B_{rIV}(r, \theta) K_{dpin} \sin np\theta \quad (30)$$

where the  $K_{dpon}$  and  $K_{dpin}$  are the winding factors for outer and inner stator respectively. The output torque estimated based on the back-emf for each phase can be written as

$$\tau_{output} = \frac{1}{\omega_r} (\mathcal{E}_{phase,a} i_a + \mathcal{E}_{phase,b} i_b + \mathcal{E}_{phase,c} i_c) \quad (31)$$

where the  $\mathcal{E}_{phase,a}$ ,  $\mathcal{E}_{phase,b}$ ,  $\mathcal{E}_{phase,c}$  are phase back-emfs for each phase and  $i_a$ ,  $i_b$ ,  $i_c$  are phase current excitation, and  $\omega_r$  is a motor speed.

## FINITE ELEMENT ANALYSIS AND VALIDATION

The electromagnetic characteristics and performance of electrical machines are commonly modelled and predicted using finite element analysis (FEA). For further comparative evaluation, 2D finite element (FE) models are built for the exact motor geometry and dimensions of DS-PMSM as used in the analytical subdomain model (ASDM). FE commercial software, Ansys Maxwell is employed for this 2D FE modelling and results from

the FE model are tabulated, plotted and compared with that of the ASDM. The comparison of airgap flux density distributions at mid airgaps are shown in Figure 3(a) for outer air-gap and Figure 3(b) for inner air-gap. Both figures show the radial and tangential components of the flux density waveforms. Both FEA and ASDM results yield approximately consistent waveform with similar amplitude and shape, which verifies the accuracy of the analytical method. The effect of stator slotting, clearly visible as indicated by the spikes in the waveforms, can be accounted for quite accurately by ASDM.

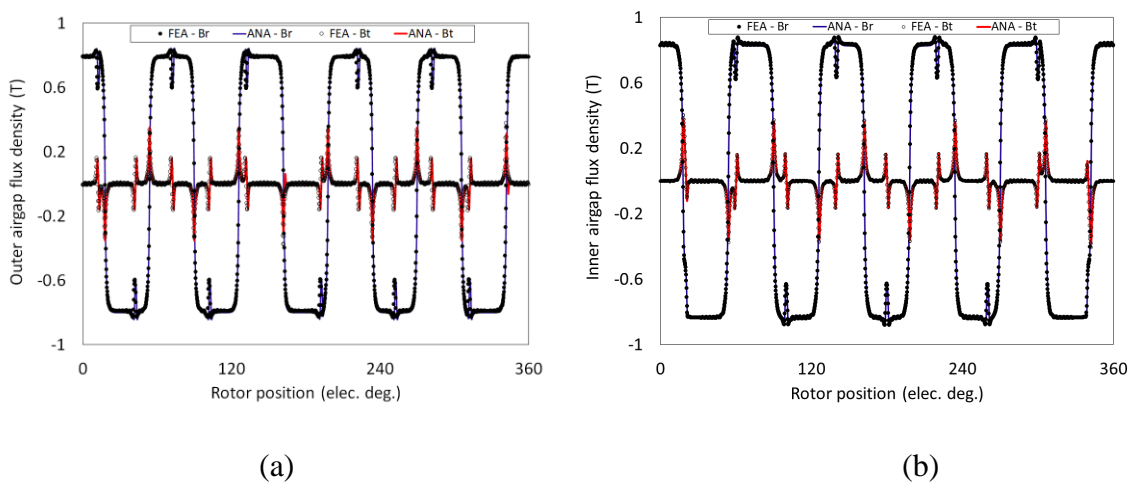


**Figure 3** Radial and tangential components of airgap flux density waveforms (a) outer airgap (b) inner airgap.

This double-stator PM motor features a non-overlapping winding type, concentrated in both the outer and inner stator slots. Due to the stator-to-rotor ratio being different between the outer and inner parts, the induced back-emf waveforms are also not in phase between the outer and inner stator. To achieve phase alignment, the rotor position can be shifted to synchronize the back-emf waveforms for each phase between both stators.

The total phase back-emf for DS-PMSM is a combination of outer and inner phase back-emfs as shown in Figure 4(a). The waveforms also shows all phases of A, B and C. The difference in electrical displacement angles between the waveforms is  $120^{\circ}$  electrical indicating that the winding configuration between the outer and inner stator slots is appropriately connected. The motor generates a smooth three-phase sinusoidal waveform.

Furthermore, Figure 4(b) illustrates the line back-emfs i.e. AB, BC and CA line-to-line back-emf waveforms.

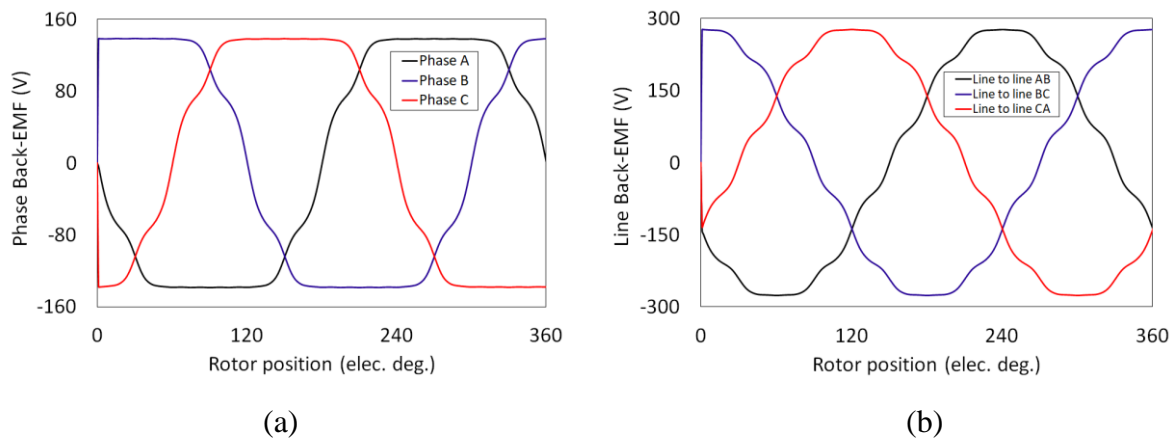
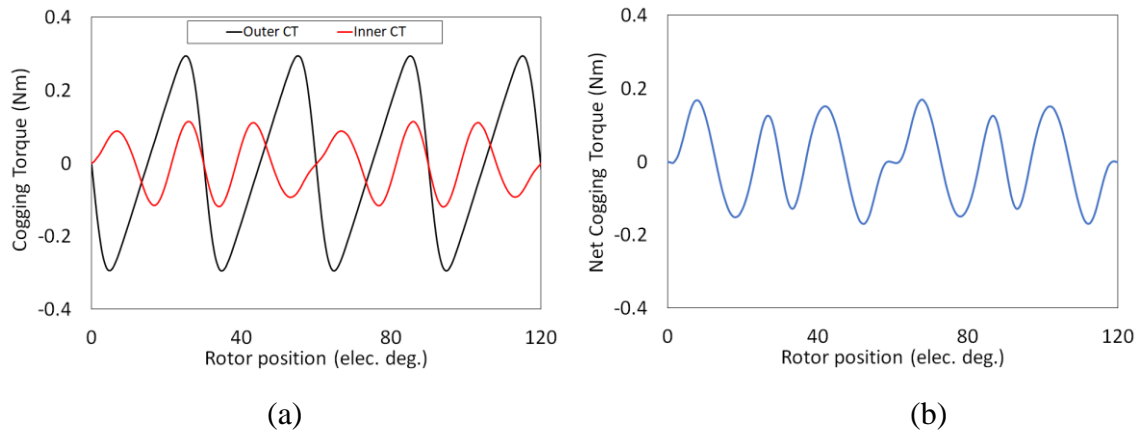


**Figure 4** Back-emf waveforms (a) Phase back-emf (b) Line back-emf

One advantage of designing brushless machines with a fractional slot-pole configuration is that the machines can have relatively low cogging torque. Reduced cogging torque efficiently reduces torque ripple, vibration, and noise produced by the motor during operation. Cogging torque can be comparatively low for the twin stator motors mentioned in this work since both the inner stator slot and outer stator slot to pole combinations are fractional.

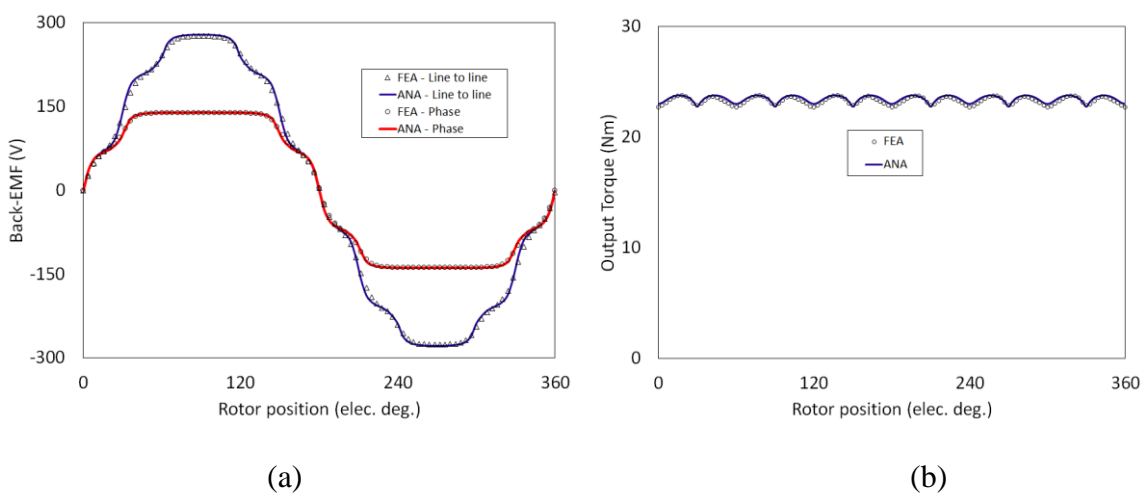
Due to the fact that the proposed DS-PMSM includes a 12-slot/10-pole for outer section and a 9-slot/10-pole for inner section, the smallest common multiples for each part are 60 and 90, respectively. As a result, the cogging torque waveform is repeating every 30 degree electrical for outer cogging torque and 60 degree electrical for inner cogging torque.

Figure 5(a) shows the cogging torque waveforms obtained from both outer and inner stator part simulated by 2D FEA. It can be observed that magnitude of the outer stator cogging torque is around 0.32 Nm and the inner stator cogging torque is around 0.12 Nm. Figure 5(b) shows the magnitude of the net cogging torque generated by the double stator motor which combines both outer and inner cogging torques. The magnitude of the net cogging torque is around 0.16 Nm. As can be seen, the net cogging torque in double stator motor can be significantly reduced around 50% compared to outer cogging torque.



**Figure 5** Cogging torque waveforms (a) Outer and Inner Cogging Torque (b) Net Cogging Torque

Figure 6 indicate the results of a comparison of analytically predicted and FEA-simulated findings. Figure 6(a) illustrates the phase and line back-emf waveforms, whereas Figure 6(b) illustrates the output torque waveforms under sinusoidal current excitation (b). As a result of these findings, it is clear that the proposed analytical subdomain model for DS-PMSM exhibits great agreement. The analytical results are remarkably similar to those obtained using FEA under open circuit and onload conditions.



**Figure 6** Motor output performance (a) Phase and line back-emf waveforms (b) Output torque waveform

The output performance of the DS-PMSM motor is given in Table 2 from both the FEA model and the analytical mode. The error is less than 1% for all categories of motor outputs. For instance, the error is about 0.13% between the ASDM and FE in magnitude of outer airgap flux density. It is about 0.69% error in average output torque. Each output performance shows a very small difference between ASDM and FEA. Therefore, the accuracy of the analytical model in estimating the performance of three-phase DS-PMSM is quite reliable and effective.

**Table 2.** Comparison of Output Performance

<b>Output Data</b>	<b>FEA</b>	<b>Analytical</b>	<b>Error (%)</b>
Maximum Outer airgap flux density, $B_{og}$ [T]	0.792	0.793	0.13
Maximum Inner airgap flux density, $B_{ig}$ [T]	0.836	0.837	0.12
Maximum line-line back-emf, $\mathcal{E}_{line}$ [V]	276.6	278.4	0.65
Maximum phase back-emf, $\mathcal{E}_{phase}$ [V]	138.6	139.29	0.5
Average output torque, $T_o$ [Nm]	23.29	23.45	0.69
Average output power, $P_o$ [W]	1465.9	1475.9	0.68

## CONCLUSION

An analytical subdomain model has been presented for predicting the magnetic field distributions during open circuit and onload conditions in three-phase DS-PMSM. Compared to 2DFEA analysis, the analytical results show excellent agreement. Because of the high accuracy of the proposed analytical subdomain model, it is possible to effectively evaluate the performance of DS-PMSM in a much shorter computational time.

## ACKNOWLEDGMENT

The authors would like to thank Ministry of Higher Education Malaysia for the financial support under FRGS Grant Scheme with Project Number FRGS/1/2021/TK0/USM/02/31

## REFERENCES

- Ahmad, Mohd Saufi, Dahaman Ishak, and Mohd Rezal Mohamed. 2020.** “Comparative Evaluation of Three-Phase Double Stator Pmsm with Different Slot Number in Inner and Outer Stators.” *International Journal of Advanced Science and Technology* 29(6 Special Issue): 783–93.
- Ahmad, Mohd Saufi, Dahaman Ishak, Tiang Tow Leong, and Mohd Rezal Mohamed. 2021.** “Optimization of Double Stator Pmsm with Different Slot Number in Inner and Outer Stators Using Genetic Algorithm.” *International Journal of Power Electronics and Drive Systems* 12(2): 726–35.
- Akmar Mohd-Shafri, Syauqina et al. 2020.** “Investigation the Optimum Performance of the Surface-Mounted PMSM under Different Magnetization Patterns.” *Journal of Physics: Conference Series* 1432(1): 1–8.
- Asef, Pedram, Ramon Bargallo Perpina, Saeed Moazami, and Andrew Craig Laphorn. 2018.** “Rotor Shape Multi-Level Design Optimization for Double-Stator Permanent Magnet Synchronous Motors.” *IEEE Transactions on Energy Conversion* 34(3): 1223–31.

**Awah, C. C. et al. 2016.** “Comparison of Partitioned Stator Switched Flux Permanent Magnet Machines Having Single- or Double-Layer Windings.” *IEEE Transactions on Magnetics* 52(1).

**Edhah, Saleh O., Jamal Y. Alsawalhi, and Ahmed A. Al-Durra. 2019.** “Multi-Objective Optimization Design of Fractional Slot Concentrated Winding Permanent Magnet Synchronous Machines.” *IEEE Access* 7: 162874–82.

**Gul, Warda, Qiang Gao, and Wanchak Lenwari. 2020.** “Optimal Design of a 5-Mw Double-Stator Single-Rotor Pmsg for Offshore Direct Drive Wind Turbines.” *IEEE Transactions on Industry Applications* 56(1): 216–25.

**Ling, P. P., Dahaman Ishak, and T. L. Tiang. 2017.** “Influence of Magnet Pole Arc Variation on the Performance of External Rotor Permanent Magnet Synchronous Machine Based on Finite Element Analysis.” *PECON 2016 - 2016 IEEE 6th International Conference on Power and Energy, Conference Proceeding*: 552–57.

**Mohamed, M. R., and D. Ishak. 2019.** “Optimization of Surface-Mounted Permanent Magnet Brushless AC Motor Using Analytical Model and Differential Evolution Algorithm.” *70(7)*: 145–51.

**Tiang, Tow Leong, Dahaman Ishak, Chee Peng Lim, and Mohamad Kamarol Mohd Jamil. 2015.** “A Comprehensive Analytical Subdomain Model and Its Field Solutions for Surface-Mounted Permanent Magnet Machines.” *IEEE Transactions on Magnetics* 51(4).

**Wang, Huimin et al. 2020.** “Optimal Design of Permanent Magnet Structure to Reduce Unbalanced Magnetic Pull in Surface-Mounted Permanent-Magnet Motors.” *IEEE Access*

8: 77811–19.

**Wang, Jiabin, Xibo Yuan, and Kais Atallah. 2013.** “Design Optimization of a Surface-Mounted Permanent-Magnet Motor with Concentrated Windings for Electric Vehicle Applications.” *IEEE Transactions on Vehicular Technology* 62(3): 1053–64.

**Wang, Zheng et al. 2019.** “A Dual-Channel Magnetically Integrated EV Chargers Based on Double-Stator-Winding Permanent-Magnet Synchronous Machines.” *IEEE Transactions on Industry Applications* 55(2): 1941–53.

**Wu, D., and Z. Q. Zhu. 2015.** “Design Tradeoff between Cogging Torque and Torque Ripple in Fractional Slot Surface-Mounted Permanent Magnet Machines.” *IEEE Transactions on Magnetics* 51(11): 16–19.

**Yang, Yee Pien, and Ming Tsan Peng. 2019.** “A Surface-Mounted Permanent-Magnet Motor with Sinusoidal Pulsewidth-Modulation-Shaped Magnets.” *IEEE Transactions on Magnetics* 55(1).

**Zhao, Wenliang, Zhishuo Yang, Yan Liu, and Xiuhe Wang. 2021.** “Analysis of a Novel Surface-Mounted Permanent Magnet Motor with Hybrid Magnets for Low Cost and Low Torque Pulsation.” *IEEE Transactions on Magnetics* 57(6): 3–6.

**Zhu, Xinkai, and Ming Cheng. 2019.** “Design and Analysis of 10 MW Class HTS Exciting Double Stator Direct-Drive Wind Generator with Stationary Seal.” *IEEE Access* 7: 51129